Coseismic rupture model and tectonic implications of January 7, 2022, Menyuan Mw 6.6 earthquake constraints from InSAR observation and field investigation

Yongsheng Li[1,2], Wenliang Jiang[1,4] , Yujiang Li[1*], Wenhao Shen[1], Zhongtai He[1], Bingquan Li[3], Qiang Li[1,4,] Qisong Jiao[1,4], Yunfeng Tian[1,4]

[1] National Institute of Natural Hazards, Ministry of Emergency Management of China, Beijing 100085, China

[2] Key Laboratory of Landslide Risk Early-Warning and Control, MEMC, Chengdu 610059, China

[3] School of Automation, China University of Geoscience, Wuhan, 430074, China

[4] Key Laboratory of Emergency Satellite Engineering and Application Ministry of Emergency Management, Beijing,100124,China

Corresponding author: Yujiang Li (yujiangli@ninhm.ac.cn)

Key Points:

- The Coseismic deformation maps of 2022 Menyuan earthquake were obtained.
- The strain energy in the eastern Tuolaishan fault may not be fully released.
- Seismic risk of the Tianzhu seismic gap is further strengthened.

Abstract

A Mw 6.6 earthquake struck Menyuan, Qinghai, China, on January 7, 2022. To determine the rupture parameters and the seismogenic environment, we resolve the optimal rupture parameters and discuss the tectonic implications of this earthquake event. The Coseismic InSAR deformation maps suggested a maximum of ~80 cm distributed in the light-of-sight direction of the satellite on the southern side of the fault and a maximum of ~70 cm on the northern side. We further estimated the focal mechanism by building a two-segment sinistral strike-slip fault model. The best-fitting solution emphasized that the 2022 Menyuan earthquake ruptured at the junction of the Tuolaishan fault and the Lenglongling fault. Both rupturing faults were dominated by the sinistral strike-slip, and the main slip was concentrated at the shallow part of the rupture plane. The latter is the main rupture segment with a strike of 106° and a dip of 86°. The slip has mainly occurred at depths of 0-8 km, and the rupture was exposed to the surface. The maximum slip reached ~3.5 m, which was mainly distributed at a depth of 4 km. Jointed analysis of optimal slip model, relocated aftershocks, Coulomb stress change, and field observation suggested that the strain energy in Tuolaishan fault may not be fully released and needs further attention. Moreover, the 2022 Mw6.6 Menyuan earthquake caused a significant stress loading effect on the western Tuolaishan fault and eastern Lenglongling fault, which implied that the 2022 event had strengthened the seismic risk in these regions.

1 Introduction

On January 7, 2022, a Mw 6.6 earthquake occurred in Menyuan, Qinghai, China (37.77°N, 101.26°E), and the depth of the hypocenters was 10 km. The epicenter was located in the high mountainous area on the southern border of Qilian Mountain on the northeastern Qinghai-Tibet Plateau (QTP) (Fig. 1). The average altitude within 5 km of the epicenter is approximately 3600 m. The earthquake occurred on the Lenglongling strike-slip fault, extending westward from the Haiyuan-Laohushan fault zone to the Qilian mountain area (Gaudemer et al., 1995; He et al., 2000, 2010). The fault is mainly a sinistral strike-slip with a few reverse fault components (Jiang, 2016; Guo et al., 2019a). Near the epicenter, the Lenglongling fault (LLLF) has several branch faults, and the strike of the main fault deflects to the west to form a tensile bend. It is a section that easily accumulates elastic strain energy and releases energy to produce moderately strong earthquakes (Xu et al., 2017). A magnitude 5.9 earthquake in Menyuan in 2016 occurred 30 km east of this epicenter (Li et al., 2016), and a Mw 8.0 earthquake in Gulang, Gansu Province occurred in 1927 near this epicenter (Jiang, 2016; Xu et al., 2022; Guo et al., 2019b). After an earthquake, exploring slip models and rupture parameters of the fault is critical to investigate the geological structures and assess potential earthquake hazards models. Many solutions for the focal mechanisms of this earthquake have been obtained using different methods and data sources (Tab. S1). These focal mechanisms have a certain degree of uncertainty, which causes difficulties in seismic dynamic analysis and other applications. The rapid products of focal mechanism for most earthquakes were inverted from the seismic-wave data. Generally, these products will employ single fault model for fast inversion. For some moderate-strong earthquakes, a complicated multi-fault models were necessary.

In this paper, both descending and ascending track data from Sentinel-1are employed to obtain the coseismic deformation fields of the 2022 Menyuan earthquake (Fig. 1). Then, a further inversion is employed to estimate the key parameters, such as rupture geometry and slip distribution characteristics. With the constraints from the fields investigation, the seismic ruptute zone and stress release were detailed analyzed. The 2016 and 2022 earthquake events offered another chance to better explore the formation mechanisms and seismotectonic of the LLLF zone and nearby regions, which have great significance in assessing the recent trend of large earthquake activity on the NE QTP.

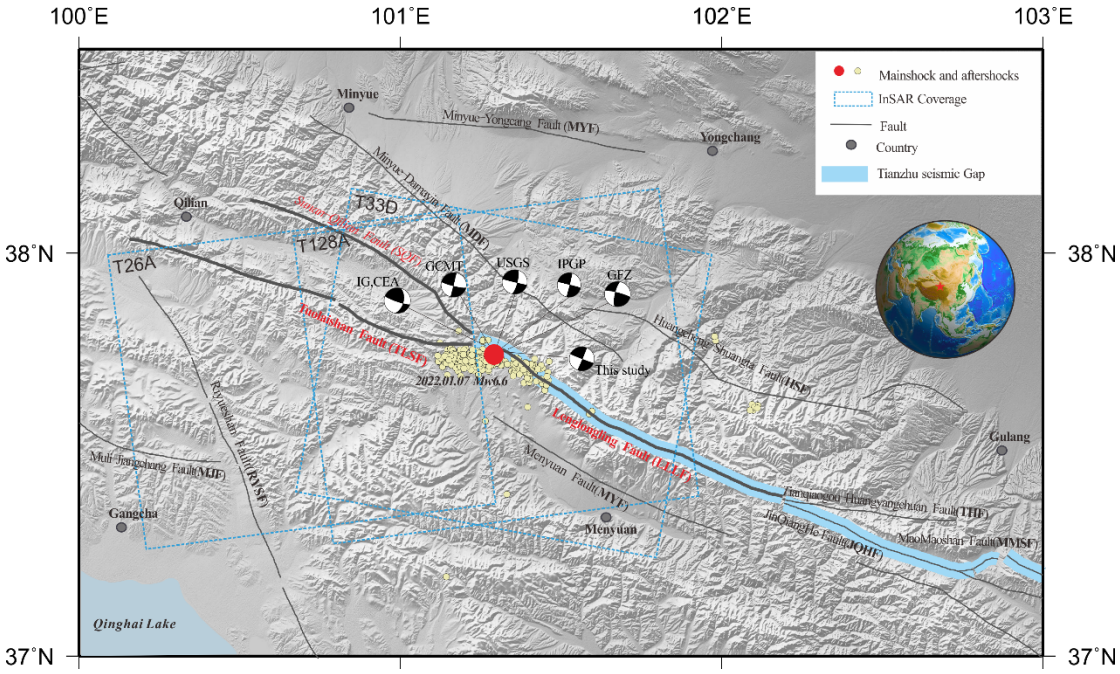

Figure 1. Active faults and seismotectonic background of the region surrounding the 2022 Menyuan earthquake, the faults are referred from Deng et al., 2007; Xu et al., 2017. The yellow points indicate the aftershock (Fan et al., 2022).

2. Tectonic setting

The LLLF zone is an intraplate region located on the northern margin of the QTP and exhibits left-lateral and oblique-slip along its western segment during the Quaternary (Fig. 1) (Gaudemer et al., 1995). The LLLF zone is developed along the watershed of the Qilian Mountains, with a strike of N110º-115ºE and an overall extension of more than 120 km (Jiang, 2016). This fault zone is connected to the Huangyangchuan fault and the Jinqianghe fault to the east. The western end is connected to the Qilian-Sunan fault zone and Tuolaishan fault (TLSF)(Fig. 1). Current research suggests that the fault was very active during the Holocene, forming many large-scale fault landforms on the surface, such as gullies, terraces, ridges, and moraines distributed along the fault zone, and some synchronous left-handed faults are distributed in many typical areas (Gaudemer et al., 1995; 2002; He et al., 2000, 2010).

The behaviors of this earthquake were consistent with other earthquake events that occurred in or near the Haiyuan fault system (Xu et al., 2017). This event occurred in the strike-slip compression zone corresponding to the bend of the LLLF zone. Until January 17, 2022, more than 500 aftershocks had occurred (Fig. 1), and the maximum aftershock moment magnitude was M 5.3. These aftershocks were mainly located approximately 40 km along the rupturing fault. The aftershocks located on the western end of the rupture reflected a near east-

west fault and were consistent with the nearly east-west strike of the TLSF. In contrast, the aftershocks on the eastern side of the rupture were mainly distributed along the LLLF. Thus, both the LLLF and TLSF may contribute to this earthquake event. No Mw>7.0 earthquake has been recorded on the LLLF zone. However, two Mw 5.9 earthquakes occurred in the LLLF zone on August 26, 1986, and January 21, 2016 (Li et al., 2016). The present-day activity rate is approximately 6.6±0.3 mm/year, and the earthquake recurrence interval is approximately 1430±140 years (Jiang, 2016), which were roughly consistent with the fault recurrence interval in the eastern section of the NE QTP (Zheng et al. 2013; Liu-zeng et al., 2007). Whether the two earthquakes that occurred in 2016 and 2022 imply the breakage of the Tianzhu seismic gap and whether a larger earthquake will occur should be given more attention (Gaudemer et al., 1995).

3. InSAR coseismic deformation

3.1 InSAR data and methodology

To characterize the coseismic deformation fields of the 2022 Menyuan earthquake event, this paper adopted three Sentinel-1 pairs (T26, T33, and T128) with ascending and descending tracks (Fig. 1 and Tab. S2) and an automatic seismic deformation InSAR monitoring system (Li et al., 2021). ALOS World 3D with the 30-meter resolution was employed as external DEM data to eliminate the phase contribution of terrain turbulence (Tadono et al., 2014). To suppress the noise and improve the signal-to-noise ratio (SNR), multilook processing with a factor of 10:2 was adopted in interferometric processing. The minimum cost flow (MCF) method was employed to unwrap the phase (Chen et al., 2000). We estimated a linear function with the observation data in the far-field nondeformation region to remove the orbital residual (Li et al., 2020). After eliminating the possible error contribution, the final coseismic deformation fields were obtained (Fig. 2).

3.2 Coseismic deformation

The sinistral strike-slip trend of The LLLF is nearly east-west. In addition, the epicenter is located on the northwestern edge of the QTP, with a dry climate and sparse vegetation, so it shows very high coherence on the interferograms (Fig. 2). The coseismic deformation fields of three tracks demonstrated that this earthquake produced a conspicuous butterfly-shaped pattern and revealed complex surface deformation characteristics (Figs. 2(b)(c)). From the results of different track data, the two walls showed opposite deformation trends, which is consistent with the concept that this earthquake was a rupture event dominated by sinistral strike-slip faults. Moreover, we found a noticeable loss of coherence in the meizoseismal region. The reason for this phenomenon is that the thick snow coverage reduced the coherence of the interferogram. In addition, the rupture deformation gradient near the epicenter exceeded the deformation monitoring resolution of the Sentinel-1 satellite, resulting in the discontinuity of the deformation phase. Nevertheless, the interferograms well describe the overall

deformation characteristics of the earthquake. The results from the descending track 33 confirmed that the maximum LOS deformation is approximately 70 cm and 80 cm, respectively in the northern and southern sides of the interred faults (Fig. 2(b)), while is approximately 40 cm and 60 cm, respectively, in the ascending path 128 (Fig 2(c)). These deformations are mainly concentrated at the junction of LLLF and TLSF, which implies that the eastern section of the TLSF and the western section of the LLLF ruptured simultaneously.

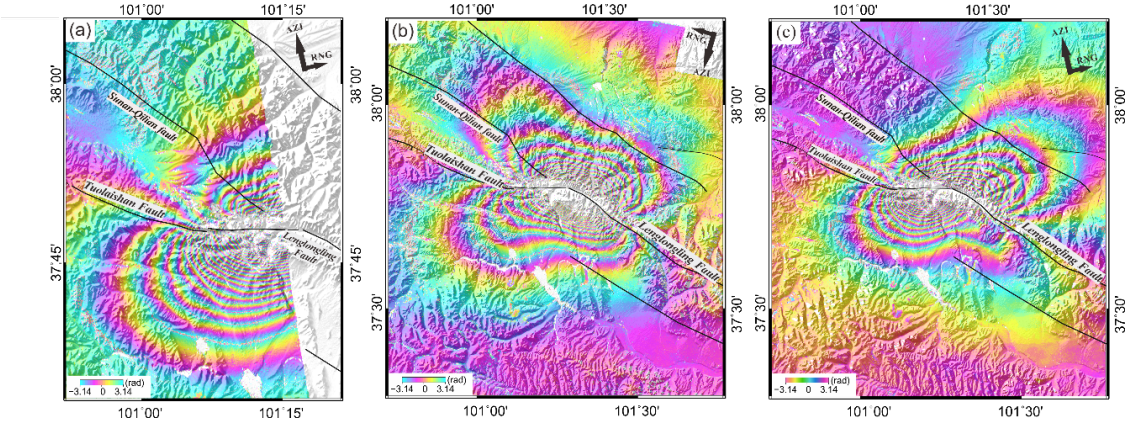

Figure 2. (a) Coseismic deformation of 2022 Menyuan quake event derived from Sentinel-1ascending track 26. (b) Coseismic deformation fields from descending track 33. (c) Coseismic deformation fields from ascending track 128. The black dotted lines indicate faults distributed near the epicenter.

4. Focal mechanism inversion

4.1 Determination of the surface rupture fault

According to the field investigation, this earthquake caused many significant surface ruptures. The interpretation results from Gaofen-7 satellite images indicated that the surface rupture length is more than 20 km (Li et al., 2022). In this paper, the pixel offset tracking (POT) method (Wang et al., 2018) and Sentinel-1 descending track 33 images were employed to explore the surface rupture zone. The results provided an essential constraint for the inversion of this earthquake, especially their strike parameters (Fig. 3). The results showed that azimuth deformation is not apparent (Fig.3(a)). In contrast, the deformation in the range direction was intense (Fig.3(b)), which also validates the characteristics of the E-W strike-slip. According to the interpretation of the POT results, the western segment of the inferred rupture coincides with the LLLF zone, while the eastern segment overlaps with the TLSF. Therefore, the rupture process of this earthquake resulted from the joint action of the two faults.

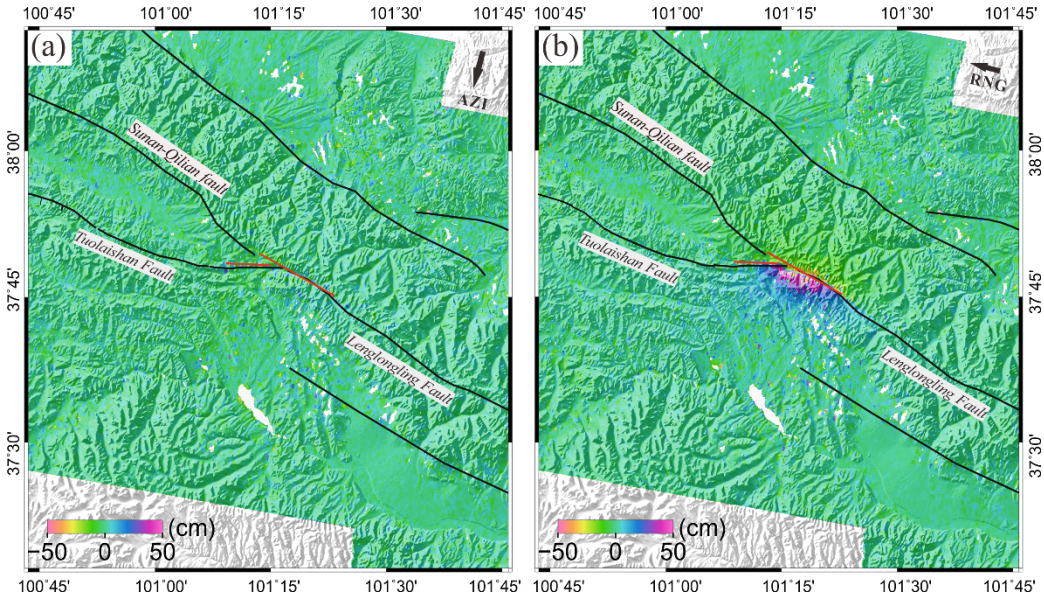

Figure 3. Rupture faults are determined by pixel offset tracking, (a) deformation in the azimuth direction and (b) deformation in the range direction. The red lines indicated inferred rupture faults.

4.2 Uniform slip model

Since the ascending track 128 and descending track 33 can completely cover the whole deformation field of this earthquake event (Figs. 2(b)(c)), we selected them as the observation constraints for further inversion processes. The elastic half-space rectangular dislocation theory was applied to the inverse uniform slip of this earthquake (Okada, 1985). By comprehensively considering the overall distribution of the aftershock sequence (Fig. 1), the characteristics of the co-seismic deformation interferogram (Figs. 2(b)(c)), and the focal mechanism solutions resolved by other sources (Tab.S1), we constructed a uniform slip model with two near east-west sinistral strike-slip planes. A rupture model with two hypothetical faults was constructed to be responsible for this earthquake. They represented the LLLF and TLSF (Fig. 3(b)), and we assumed that the strikes of the faults ranged from 105° and 120° and from 80° and 100°, respectively. These faults are high dipping sinistral strike-slip faults, so we set dip angles ranging from 80° to 89° and slip angles ranging from -20° to 20°. The particle swarm optimization method was adopted to seek the optimal location, strike, dip angle, slip angle, fault width, length, burial depth of the upper boundary of the fault, and slip amount (Feng et al., 2013). To evaluate the uncertainties of the nonlinear inversion, the gaussian errors were add to the original observations. Then, we estimated the trade-offs for the geometric parameters by a Monte Carlo analysis with 100 perturbed datasets, the small uncertainties impied that the nonlinear inversion has high reliability(Fig. S1).The optimal results emphasized that this earthquake ruptured on two faults, one is a nearly

east-west sinistral strike-slip fault with a length of ~20 km, which has a minor reverse fault component (rake angle is ~-5° and strike angle of ~106°), and another is a 10 km pure east-west sinistral strike-slip fault (strike angle of ~89°).

4.3 Distributed slip model

Then, we fixed the location and strike angle of the rupture plane derived from the previous optimal rupture parameters, and the lengths and widths of the fault planes were expanded along the strike and dip, respectively. The two fault planes were discretized into a small rectangle patch with 1 km×1 km. The dip angle was further optimized in the subsequent linear inversion. We applied a LOG function to reestimate the best-fitting dip angle (Feng et al., 2013). The optimal slip models revealed that the rupturing planes were dominated by two strike-slip faults. The western section of the LLLF and the eastern section of the TLSF participated in the rupture simultaneously. The best-fitting solution suggested that the main rupture plane distributed with a strike of ~106°, a dip of ~86°, and a rake of ~-5° along the LLLF is a strike-slip fault, while the secondary rupture plane distributed along the TLSF with ~89°, ~83° and ~-1°, respectively. The fault slip is mainly distributed in the western segment of the LLLF (Fig. 4 and Fig. S2). The main slip was distributed at the shallow part of the rupture plane at depths of 0−8 km, and the maximum slip of 3.5 m is concentrated at a depth of 4 km (Fig. 5). The apparent slip amount can be observed on the shallow rupture plane (0~1 km), implying that the coseismic slip ruptured at the surface (Fig. 5). The slip distribution model produced a cumulative seismic amount of ~1.0244×10^{19} Nm, equivalent to an earthquake with Mw 6.6, consistent with the results from other sources (Tab. S1). Fig. 4 indicated that the mainshock had triggered abundant aftershocks with depths of 7−14 km, mainly concentrated below the main rupture region of this earthquake. To validate the inversion reliability, we estimated the surface deformation derived from the optimal distributed slip model and both tracks of SAR geometry. The simulated interferograms (Figs. 6(b)(e)) accurately fit the observation deformation of both tracks and can better explain the spatial distribution of the coseismic deformation field. The residuals are small (Figs. 6(c)(f)), which implies that the ruptured model estimated in this paper has high reliability.

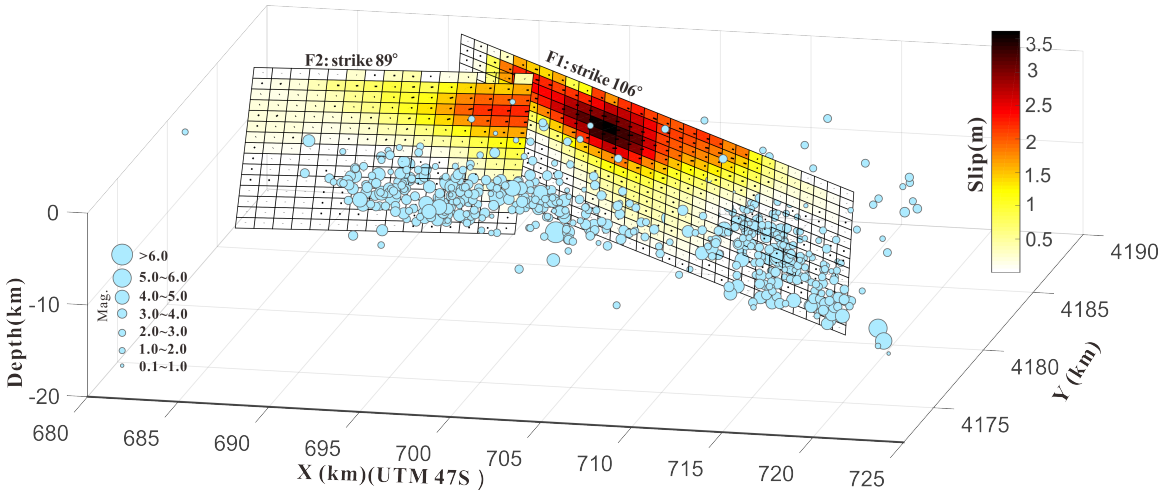

Figure 4. The slip model of the rupture faults of the 2022 Menyuan earthquake. The blue points represented the mainshock and aftershocks until January 17, 2022.

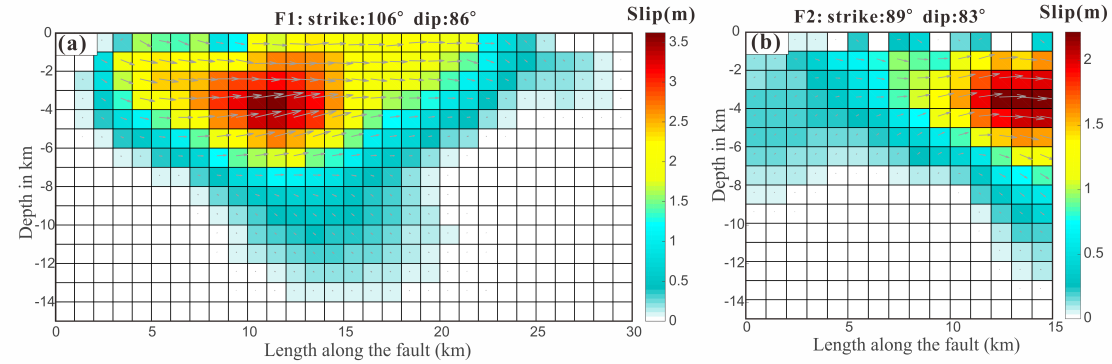

Figure 5. Optimal slip distributions of the 2022 earthquake event.

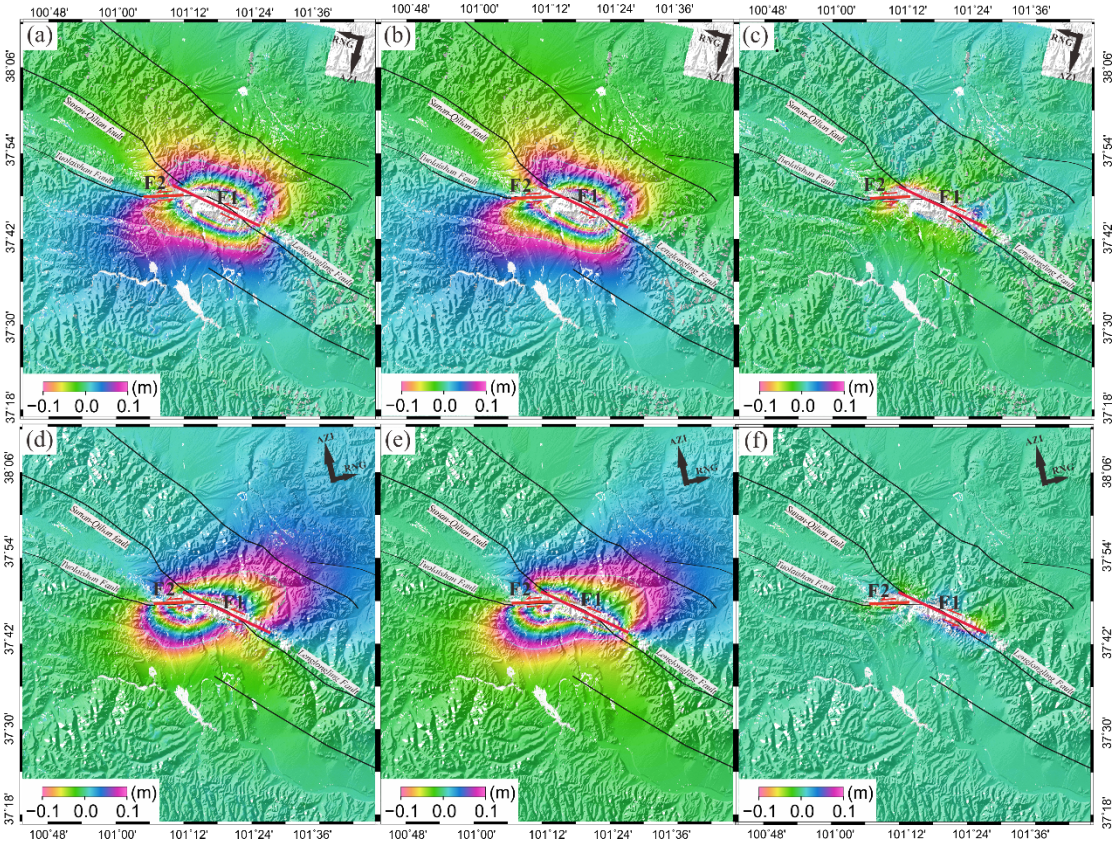

Figure 6. Coseismic deformation fields of the 2022 Menyuan earthquake. (a),(d) show the observed coseismic deformation for descending track 33 and ascending track 128, respectively. (b),(e) represent simulated deformation maps. (c),(f) represent the residuals. F1: a rupturing segment of the LLLF, F2: rupturing segment of the TLSF.

4.4 Coulomb stress changes

The Coulomb stress change(*CFS*) caused by the 2022 Menyuan earthquake is expressed as Eq.1. Positive *CFS* benefits the occurrence of succeeding earthquakes(King *et al.*, 1994).

$$\Delta CFS = \Delta\tau + \mu'\Delta\sigma_n \quad (1)$$

The coseismic *CFS* was calculated by applying the elastic dislocation model (Okada, 1985). The Burgers body was employed to simulate the viscoelastic rheological properties of the lower crust and the upper mantle (Shao *et al.*, 2016; Li *et al.*, 2020). To analyze the jointed effects of the coseismic dislocations and postseismic viscoelastic relaxation, we adopted the PSGRN/PSCMP code based on a stratified viscoelastic model (Wang *et al.*, 2006) to calculate the stress changes. Based on the lithosphere's velocity structure and rheological

properties around the NE QTP (Shao *et al.*, 2007; He *et al.*, 2013; Liu *et al.*, 2019;), we determined the parameters in the viscoelastic stratified model, as shown in Tab. S3.

We calculated the coseismic *CFS* associated with the 2022 Mw6.6 Menyuan earthquake by projecting the stress tensors to the focal parameters of the mainshock. The effective friction coefficient is set as 0.4. Fig. 7 shows the projection results of static *CFS* at depths of 5km and 10 km on the optimal rupture surface caused by the 2022 Menyuan Mw6.6 earthquake. We can find that the occurrence of the mainshock caused significant changes in *CFS* on un-ruptured parts of the LLLF, the TLSF, and some parts of the Minle-Damaying fault (Fig. 7). Thus, it has increased the seismic hazard of these faults along the Tianzhu seismic gap, but the significant stress decrease on most sections of the Minle-Damaying fault, the Huangcheng fault, the Menyuan fault and the eastern segment of the Sunan-Qilian fault.

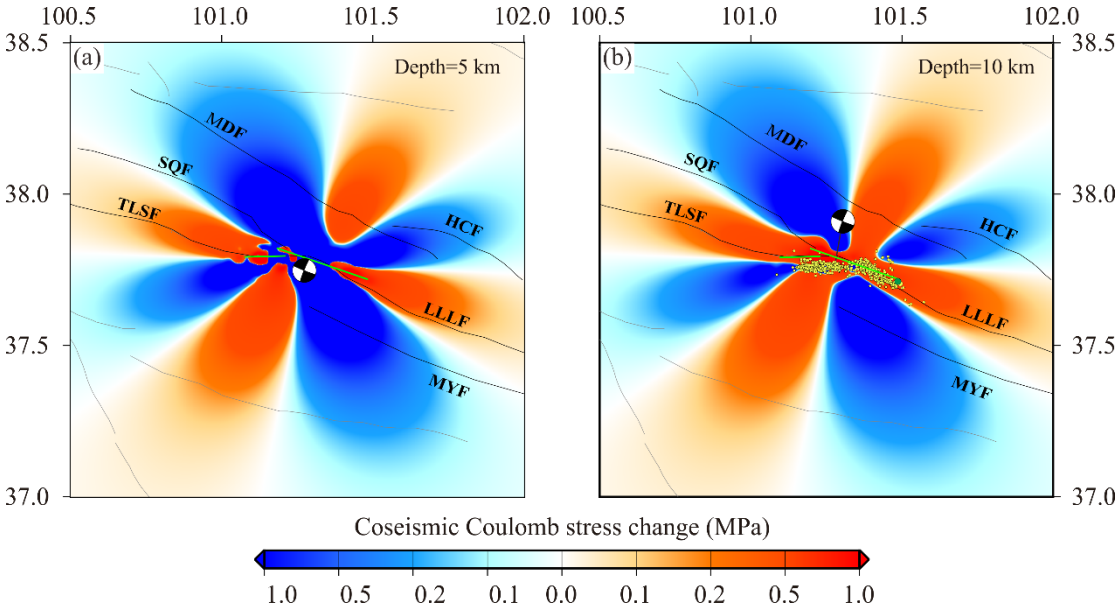

Figure 7. Coseismic CFS associated with the 2022 Menyuan Mw 6.6 earthquake at depths of 5 km and 10 km. (a) represents a depth of 5 km and (b) represents 10 km. The black lines indicate the active fault. The green lines represent the rupturing fault inferred from modelling. Yellow points indicate the relocated aftershocks, and the green dot indicates the largest M 5.3 aftershock.

5. Discussion

5.1 Seismotectonic model of the LLLF zone

The QTP is formed and developed is under continuous collision between the Indian and Eurasian Plates. The oblique movement between the Indian Plate and the Eurasian Plates has caused interactions at the edge of the plateau, which

has also led to the occurrence of Earthquake-prone faults. The 2022 Menyuan earthquake occurred on an east-west-trending sinistral fault within the Qilian-Haiyuan tectonic belt. It comprises several active sinistral strike-slip active fault zones with WNW-ESE strikes and oblique echelon arrangements. These fault zones play a crucial role in regulating and transforming the tectonic deformation in the northeastern QTP (Jiang, 2016; Guo et al., 2019a,2019b).

The GPS velocity fields and strain rates (Liang et al., 2013) suggested the structural deformation on the northeastern margin of the QTP rotates clockwise due to the obstruction of the Ordos and Gobi-Alashan blocks. The direction gradually changes from NE thrusting in the west to sinistral strike-slip along the Qilian-Haiyuan structural belt, and the strain direction changes to SEE to SSE (Fig. 8). Along the Qilian-Haiyuan structural belt, the deformation gradually transitions to sinistral strike-slip, especially in the LLLF zone. According to the Holocene fault landform analysis, the displacement of a single earthquake event in the western section of the LLLF zone is significantly lower than that in the eastern section. In the westernmost section of the Qilian-Haiyuan structural belt, the near-parallel TLSF zone and Qilian-Sunan fault zone mainly regulate regional tectonic deformation by obvious thrusting. The cumulative displacement distribution along the fault zone increases significantly from west to east, indicating that the western section of the LLLF zone is dominated by compressive and shear tension (e.g., 2016 Menyuan earthquake), while the eastern segment of the LLLF zone exhibits sinistral strike-slip movement, which suggests that the LLLF zone plays an important role in adjusting the tectonic deformation in the NE QTP.

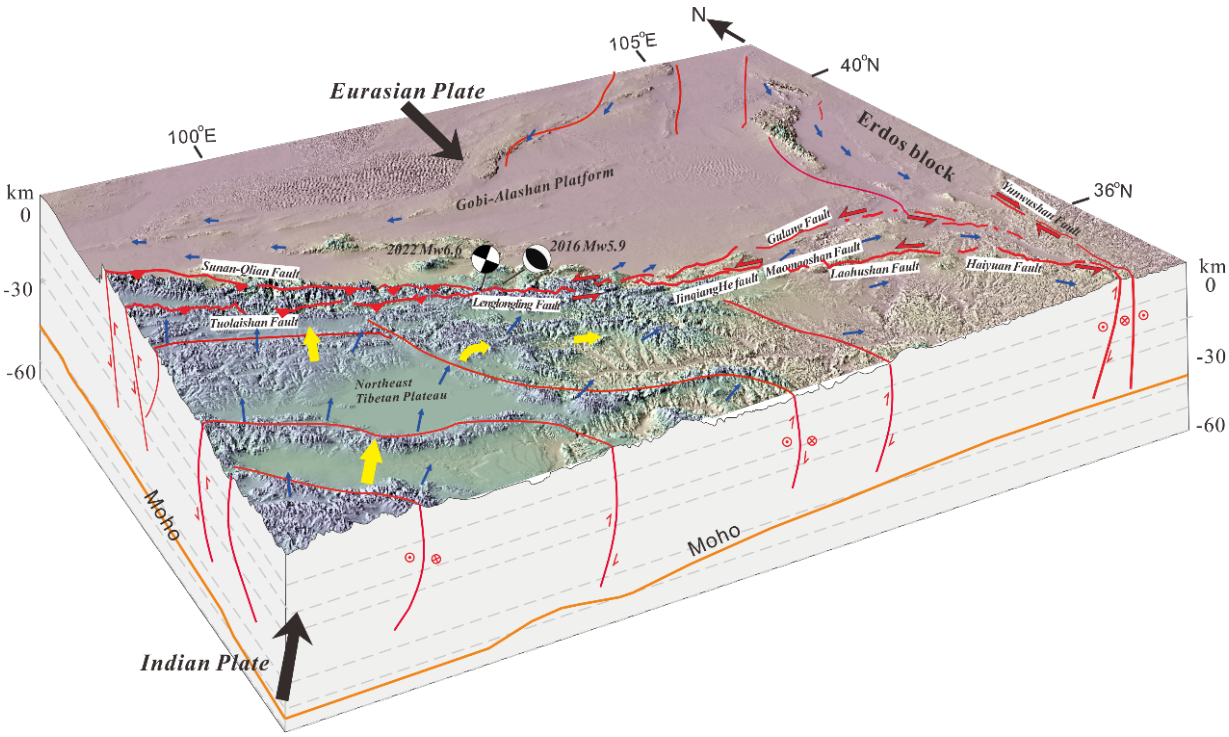

Figure 8. Comprehensive seismotectonic model of the LLLF zone and its surrounding area. The thick yellow arrows indicate the direction of plate movement. The narrow blue arrow indicates the GPS velocity field with the Gobi-Alashan block referenced from Liang et al., (2013). Profiles of the Haiyuan and Yunwushan fault zones referenced from Tang et al., (2015). Profiles of the Tuolaishan and Qilian-Sunan fault zone referenced from Yuan et al., (2013) and Liu et al., (2021). Moho depth referenced Pan and Niu, (2011) and Wang et al., (2014).

5.2 Possible triggering effect between the 2016 and 2022 events

After a strong earthquake, the stress state in the seismogenic area will be changed, which will promote or delay the occurrence of subsequent earthquakes on active faults in adjacent areas (Li *et al.*, 2020; Nalbant *et al.*, 2002; Stein, 1999; Xiong *et al.*, 2010). Around the source region of the Mw6.6 Menyuan earthquake in 2022, there occurred Mw 5.9 Menyuan earthquake in 2016. Considering that the distance between them is approximately 30 km, we further analyze the possible triggering effect between these two events. With the coseismic slip model of the 2016 event as the source rupture model (Li *et al.*, 2016), we calculated the coseismic and postseismic stress change associated with the 2016 earthquake by projecting the stress tensors to the focal parameters of the 2022 Mw 6.6 main-

shock. The results show that the coseismic normal and shear stress changes at the hypocenter of the 2022 earthquake are -0.16×10^4 Pa and 0.25×10^4 Pa, respectively (Figs. 9(a)(b)), indicating the coseismic compressive effect of the rupture plane. According to Eq. 1, we can find that the 2016 Menyuan earthquake transmitted the positive Coulomb stress change to the 2022 earthquake. In particular, the coseismic Coulomb stress change reaches 0.185×10^4 Pa (Fig. 9(c)), suggesting that the 2016 Menyuan earthquake encouraged the occurrence of the 2022 earthquake, which is consistent with the concept of Li et al., (2022). Moreover, the postseimic Coulomb stress change is positive, but the impact is limited (Fig. 9(d)). Thus, we concluded that the 2016 Menyuan earthquake promoted the occurrence of the 2022 earthquake.

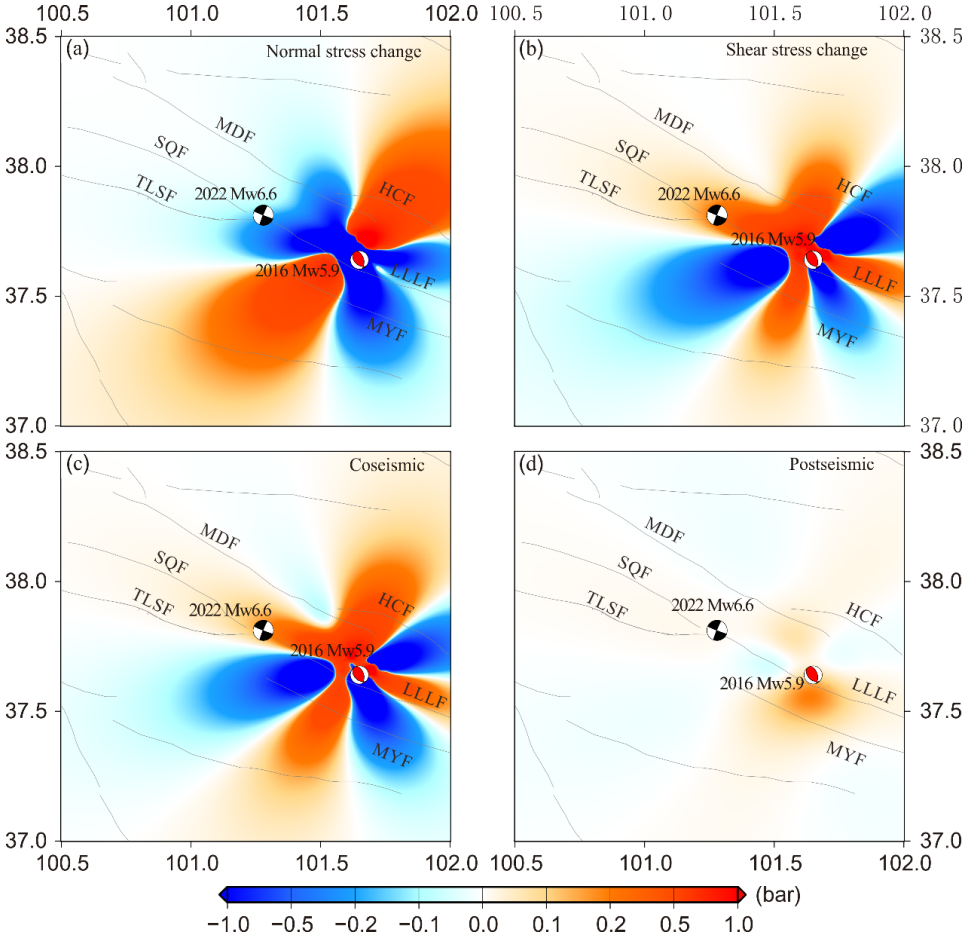

Figure 9. Stress change associated with the 2016 Menyuan earthquake. (a) represents the coseismic normal stress changes. (b) represents the shear stress

changes. (c) the coseismic Coulomb stress change. (d) the postseismic Coulomb stress change.

5.3 Whether the Coulomb stress was completely released in depth by 2022 event?

Based on the previous optimal slipe model (Fig. 5), the *CFS* caused by the mainshock of the 2022 event was calculated (Fig. 7). The statistical results show that 95% of aftershocks were distributed where Coulomb stress increases(depth=10 km). In particular, as the remarkable slip is mainly concentrated at 3−5 km (Fig. 5), the seismogenic fault may fully release the accumulated strain energy, as indicated by the significant decrease of coseismic *CFS* at a depth of 5 km near the hypocenter (Fig. 7(a)). However, at 10 km depth, because the seismogenic fault only released the partial strain energy, almost all the source region still expresses the significant increase of coseismic stress change (Fig. 7(b)). This significant stress increase well explains the occurrence of the clustering aftershocks that mainly concentrate at depths of 8−13 km (Fig. 4). Furthermore, the largest M 5.3 aftershock was occurred in the region with a high coseismic stress change of 0.33×10^6 Pa, which exceeds the threshold of Coulomb stress triggering, suggesting the triggering effect between them.

5.4 The seismic risk of TLSF derived from spatial diversity of surface rupture

Due to the influence of decorrelation, InSAR technology cannot accurately obtain the deformation pattern in the vicinity of faults of this earthquake (Fig. 2). We conducted a field investigation to clarify surface deformation and the spatial diversity of the surface rupture zone. The field investigation results show that this earthquake mainly produced two surface rupture zones (Fig.10). The green dotted lines in Fig. 10 represent the surface rupture trace identified in the field investigation, consistent with the inferred trace derived from the InSAR measurement (red lines in Fig. 10). According to the field observations, we selected the small gullies, roads, and riverbanks as the identification targets and distinguished surface rupture magnitude by measuring the surface dislocation. We selected 6 sites along the Lenglengling rupture fault to demonstrate the rupture scale (a−f in Fig. 10). We found the maximum surface rupture was larger than ~270 cm at point f, suggesting that the LLLF's rupture intensity is strong. In comparison, the rupture magnitude along the TLSF zone is relatively smaller (g and h in Fig. 10). The maximum surface dislocation is approximately ~15−20 cm. Combined with the evidence that the main earthquake was initiated in the LLLF zone, we believe that the surface rupture in the eastern section of the TLSF zone is a passive rupture induced by the rupturing of the LLLF zone. The distribution and intensity of surface rupture along the TLSF are relatively limited. Combined with Fig. 7, it shows that this earthquake has a direct stress loading effect on the TLSF. The spatial diversity of the surface rupture zone suggested that the seismic risk in the TLSF will not be reduced due to the occurrence of the 2022 earthquake and should receive continuous attention.

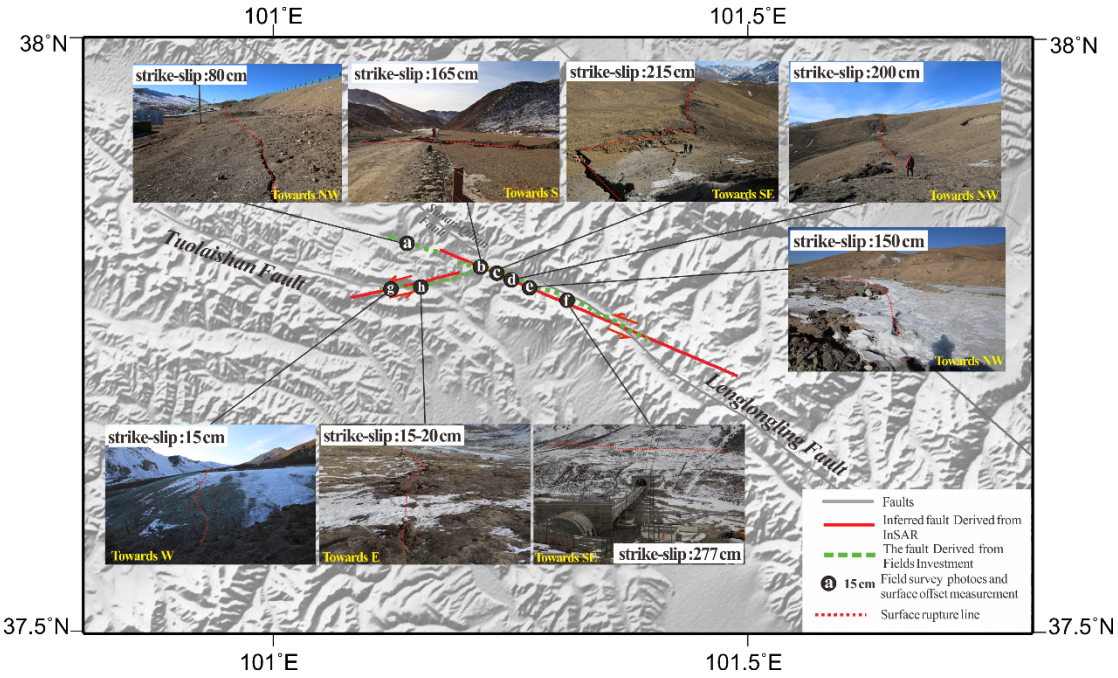

Figure 10. Surface rupture distribution derived from field measurement. Sites a—h are the selected location for field measurement of surface rupture.

6. Conclusion

The coseismic deformation maps of the Mw 6.6 Menyuan earthquake on January 7, 2022, were derived from the Sentinel-1 ascending and descending tracks. The deformation patterns demonstrated that this earthquake was dominated by a sinistral strike-slip rupturing event and revealed the complex characteristics of coseismic deformation, distributed in the junction of the western section of the LLLF and the eastern section of the TLSF. The structure geometric and optimal slip distribution of ruptured planes were obtained by employing a two-step inversion strategy. The best-fitting solution suggested that both rupturing faults were dominated by the sinistral strike-slip. The main slips were concentrated at a shallow part of the rupture planes. A combined analysis of optimal slip distribution of the 2022 event and the relocated aftershocks suggested that rare aftershocks occurred at shallow layers(<5 km), while in the deep part (10 km), strain energy may not be fully released, resulting in the aftershocks were very abundant. Jointed analysis with the coseismic and postseismic *CFS* of the 2016 event, we concluded that the 2016 earthquake encouraged the occurrence of the 2022 Menyuan earthquake. With jointing analysis of field investment, we considered that the strain energy of the TLSF might not be completely released, and its seismic risk needs further attention. To clarify the rupture parameters and tectonic implications of Menyuan earthquakes is helpful to study further the geological structure and kinematic mechanism of the LLLF and the earthquakes

risk in the Tianzhu seismic gap.

Acknowledgments

This research is partly supported by research grants from the National Institute of Natural Hazards, MEMC (grant numbers No. ZDJ 2019-17); National Key Research and Development Program of China(2021YFC3001903); Gaofen earthquake monitoring and emergency application demonstration (phase II) (31_Y30F09-9001-20/22) and the National Natural Science Foundation of China (no. 41704051, 41874116,41772219); We thank Prof. Wanpeng Feng for his PSOKINV software and constructive comments, thank The ESA for the Sentinel-1A data and thank Dr. Fan Lihua for the relocated aftershocks.

Data Availability

The focal mechanism from IG,CEA in Tab.S1 was accessed from https://www.cea-igp.ac.cn/kydt/278809.html.The Sentinel-1 SAR data were accessed form ESA(https://scihub.copernicus.eu/dhus/). Some plots were made using the Generic Mapping Tools version 4.2.1 (www.soest.hawaii.edu/gmt).

References

Burgmann, R., Ayhan, M.E., Fielding, E.J., Wright, T.J., McClusky, S., Aktug, B., Demir, C., Lenk, O., and Turkezer, A., (2002), Deformation during the November 12 1999 Duzce, Turkey, earthquake, from GPS and InSAR data: *Bulletin of the Seismological Society of America*, 92, 161-171.

Chen, C. W., Zebker, H. A., (2000). Network approaches to two-dimensional phase unwrapping: intractability and two new algorithms. *Journal of the Optical Society of America,* 17(3),401-14,https://doi.org/10.1364/josaa.17.000401

Deng, Q., Zhang, P., Ran, Y., Min, W., Yang, X., and Chu, Q., (2003). Basic characteristics of active tectonics of China. *Science in China*, 46(4), 356-372.

Fan, L., Li, B., Liao, S., Jiang, C., Fang, L.,(2022). Relocation of the mainshock and aftershock sequence of the 2022 Menyuan MS6.9 earthquake.*Earthquake Science*(in press).

Feng, W., Li, Z., Elliott, J.R., Fukushima, Y., Hoey, T., Singleton, A., Cook, R., Xu, Z., (2013). The 2011 M_W6.8 Burma earthquake: fault constraints provided by multiple SAR techniques, *Geophys. J. Int.* 195, 650–660.

Gaudemer, Y., Tapponnier, P., Meyer, B., Peltzer, G., Shunmin, G., Zhitai, C., et al., (1995). Partitioning of crustal slip between linked, active faults in the eastern Qilian Shan, and evidence for amajor seismic gap, the Tianzhu gap, on the western Haiyuan fault, Gansu (China). *Geophysical Journal of the Royal Astronomical Society,* 120(3), 599-645.

Goldstein, R. M., Zebker, H. A., and Werner, C. L.,(1988). Satellite radar interferometry: Two-dimensional phase unwrapping, *Radio Sci.*, 23(4), 713– 720, https://doi.org/10.1029/RS023i004p00713.

Guo, P., Han, Z., Dong, S., et al. (2019a). Surface rupture and slip distribution along the Lenglongling fault in the NE Tibetan Plateau: Implications for faulting behavior. *Journal of Asian Earth Sciences*, 172: 190-207.

Guo, P., Han, Z., Mao, Z., et al. (2019b). Paleoearthquakes and Rupture Behavior of the Lenglongling Fault: Implications for Seismic Hazards of the Northeastern Margin of the Tibetan Plateau. *Journal of Geophysical Research: Solid Earth*, 124(2): 1520-1543

He, W., Liu, B., Yuan, D., Yang, M., (2000), Research on slip rates of the lenglongling active fault zone.*China Earthquake engineering Journal*, 22(1), 90-97.

He, W., Yuan, D., Ge, W., Luo, H., (2010), Determination of the slip rate of the lenglongling fault in the middle and eastern segment of the Qilian mountain active fault zone, *Earthquake*, 30(1), 131-137, https://doi.org/10.3969/j.issn.1000-3274.2010.01.015

He, J., Lu, S., Wang, W., (2013). Three-dimensional mechanical modeling of the GPS velocity field around the northeastern Tibetan plateau and surrounding regions, *Tectonophysics* 584, 257-266, https://doi.org/10.1016/j.tecto.2012.03.025.

Jiang, W., (2016). Holocene Rupture Pattern, Seismic Recurrence Feature of the Lenglongling Fault Zone and Its Tectonic Implication for the Northeast Tibetan Plateau. Institute of Geology, China Earthquake Administration, Doctoral Dissertation.

King G C P, Stein R S, Lin J. (1994). Static stress changes and the triggering of earthquakes, *Bulletin of the Seismological Society of America*, 84: 935–953

Li, B., Li, Y., Jiang, W., Su, Z., & Shen, W.,(2020). Conjugate ruptures and seismotectonic implications of the 2019 Mindanao earthquake sequence inferred from Sentinel-1 InSAR data. *International Journal of Applied Earth Observation and Geoinformation*, 90, 102127. https://doi.org/https://doi.org/10.1016/j.jag.2020.102127

Li Y, Jiang W, Zhang J, Luo Y., (2016). Space Geodetic Observations and Modeling of 2016 Mw 5.9 Menyuan Earthquake: Implications on Seismogenic Tectonic Motion. *Remote Sensing*. 8(6):519. https://doi.org/10.3390/rs8060519

Li, Y., Jiang, W., Zhang, J., Li, B., Yan, R., Wang X., (2021). Sentinel-1 SAR-Based coseismic deformation monitoring service for rapid geodetic imaging of global earthquakes, *Natural Hazards Research*,1(1),1-19. https://doi.org/10.1016/j.nhres.2020.12.001

Li, Y., Shao, Z., Shi, F., Chen, L., (2020). Stress evolution on active faults in the southwestern Yunnan region, southeastern Tibetan Plateau, and implications for seismic hazard, *J. Asian Earth Sci.* 200, 104470, https://doi.org/10.1016/j.jseaes.2020.104470.

Li Z., Han B., Liu Z.,Zhang, M., Yu, C. Chen, B., Liu, H., Du, J., Zhang, S., Zhu, W., Zhang, Q., Peng, J., (2022). Source Parameters and Slip Distributions of the 2016 and 2022 Menyuan, Qinghai Earthquakes Constrained by InSAR Observations.*Geomatics and Information Science of Wuhan University*, https://doi.org/10.13203/j.whugis20220037

Liang, S., Gan, W., Shen, C., Xiao, G., Liu, J., Chen, W., et al. (2013). Three-dimensional velocity field of present-day crustal motion of the Tibetan Plateau derived from GPS measurements. *Journal of Geophysical Research:Solid Earth*, 118(10), 5722-5732.

Liu-zeng, J., Klinger, Y., Xu, X., Lasserre, C., Chen, G., Chen, W., et al., (2007). Millennial recurrence of large earthquakes on the Haiyuan fault near Songshan, Gansu province, China. *Bulletin of the Seismological Society of America*, 97(1), 14-34, https://doi.org/10.1785 /0120050118.

Liu, J., Ren, Z. K., Zhang,H., Li, C., Zhang, Z., Zheng, W., et al., (2021). Slip rates of the Laohushan fault and the along strike-slip rate spatial pattern of the Haiyuan fault zone.*Tectonics*. https://doi.org/10.1029/2021TC006992

Liu, S., X. Xu, Y. Klinger, J. M. Nocquet, G. Chen, G. Yu, and S. Jónsson, (2019). Lower crustal heterogeneity beneath the northern Tibetan Plateau constrained by GPS measurements following the 2001 Mw7. 8 Kokoxili earthquake, *J. Geophys. Res.* 124, 11992-12022, https://doi.org/10.1029/2019JB017732.

Nalbant, S. S., J. McCloskey, S. Steacy, and A. A. Barka, (2002). Stress accumulation and increased seismic risk in eastern Turkey, *Earth Planet. Sci. Lett.* 195, 291-298, https://doi.org/10.1029/98JB01491.

Okada, Y., (1985). Surface deformation due to shear and tensile faults in a half-space. *Bull. Seismol. Soc. Amer.* 75, 1135-1154.

Pan, S., and Niu, F. (2011). Large contrasts in crustal structure and composition between the Ordos plateau and the NE Tibetan plateau from receiver function analysis: *Earth and Planetary Science Letters*, 303, 291–298.

Shao, Z. G., R. S. Fu, T. X. Xue, and J. P. Huang, (2007). Simulating postseismic viscoelastic deformation based on Burgers model, *Journal of Geodesy and Geodynamics*,27, 31-37.

Shao, Z. G., J. Xu, H. S. Ma, and L. P. Zhang, (2016). Coulomb stress evolution over the past 200years and seismic hazard along the Xianshuihe fault zone of Sichuan, China, *Tectonophysics*,670, 48-65, https://doi.org/10.1016/j.tecto.20 15.12.018.

T. Tadono, H. Ishida, F. Oda, S. Naito, K. Minakawa, H. Iwamoto,(2014). Precise Global DEM Generation By ALOS PRISM, ISPRS Annals of the Photogrammetry, *Remote Sensing and Spatial Information Sciences*, II-4,71-76

Tang, J., Zhan, Y., Zhao, G., Deng, Q., Wang, J., Chen, X., Zhao, J., Xuan, F., (2005). Electrical conductivity structure of the crust and upper mantle in

the northeastern margin of the Qinghai_Tibet plateau along the profile Maqên-Lanzhou-Jingbian. *Chinese Journal of Geophysics*, 48(5): 1205-1216.

Wang, H., Gao, R., Zeng, L., Kuang, Z., Xue, A., Li, W., et al., (2014). Crustal structure and Moho geometry of the northeastern Tibetan Plateau as revealed by Sinoprobe-02 deep seismic-reflection profiling. *Tectonophysics*, 636(11), 32-39.

Wang,T.,Shi, Q., M. Nikkhoo, Wei, S., Barbot, D. Dreger, R. Bürgmann, M. Motagh, Chen,F., (2018).The rise, collapse, and compaction of Mt. Mantap from the September 3 2017 North Korean nuclear test, *Science*, 361 (6398),166-170, 10.1126/science.aar7230

Wang, K. L., Y. Hu, and J. H. He, (2012). Deformation cycles of subduction earthquakes in a viscoelastic Earth, *Nature*, 484, 327-332, https://doi.org/10.1038/nature11032.

Wang, R., F. Lorenzo-Martín, and F. Roth, (2006). PSGRN/PSCMP—a new code for calculating co-and post-seismic deformation, geoid and gravity changes based on the viscoelastic-gravitational dislocation theory, *Computers and Geosciences*,32, 527-541, https://doi.org/10.1016/j.cageo.2005.08.006.

Xiong, X., B. Shan, Y. Zheng, and R. Wang, (2010). Stress transfer and its implication for earthquake hazard on the Kunlun Fault, Tibet, *Tectonophysics* 482, 216-225, https://doi.org/10.1016/j.tecto.2009.07.020.

Xu, X., Wu, X., Yu, G., Tan, X., and Li K., (2017). Seismo-geological signatures for identifying M 7.0 earthquake risk areas and their preliminary application in mainland China, *Seismology and Geology*, 39(2), doi:10.3969/j.isn.0253-4967.2017.02.001 (in Chinese).

Xu, Y. Guo, X., Feng, L., (2022). Relocation and focal mechanism solutions of the *M*S6.9 Menyuan earthquake sequence on January 8 2022 in Qinghai Province. *Acta Seismologica Sinica* 44(2) 1-15. https://doi.org/10.11939/jass.20220008.

Yuan, D. Y., Ge, W. P., Chen, Z. W., Li, C. Y., Wang, Z. C., Zhang, H. P., et al., (2013). The growth of northeastern Tibet and its relevance to large-scale continental geodynamics: a review of recent studies. *Tectonics*, 32(5), 1358-1370.

Zheng, W. J., Zhang, P. Z., He, W. G., Yuan, D. Y., Shao, Y. X., Zheng, D. W., et al., (2013). Transformation of displacement between strike-slip and crustal shortening in the northern margin of the Tibetan Plateau: evidence from decadal gps measurements and late quaternary slip rates on faults. *Tectonophysics*, 584(1), 267-280 https://doi.org/10.1016/j.tecto.2012.01.006.